Structures 39 (2022) 1118–1134

Contents lists available at ScienceDirect

Structures

journal homepage: www.elsevier.com/locate/structures

Parametric study and improved capacity model for RC beams strengthened with side NSM CFRP bars

Ali Hadi Adheem [a], Majid M.A. Kadhim [b], Akram Jawdhari [c,*]

[a] Kerbala Technical Institute, Al-Furat Al-Awsat Technical University, 56001 Kerbala, Iraq
[b] University of Babylon, Hilla, Iraq
[c] Valparaiso University, Valparaiso, IN 46383, USA

ARTICLE INFO

Keywords:
Side near surface mounted, NSM
Concrete
Strengthening
Finite element
Parametric analysis
Design-oriented model
Debonding

ABSTRACT

Near Surface Mounted (NSM) fiber reinforced polymer (FRP) technique with rods/strips attached at the bottom face (B-NSM) has become widely used method for retrofitting concrete structures but has several practical limitations such as accessibility problems and premature debonding. A viable alternative by attaching the NSM FRP reinforcement at the side faces (S-NSM) has recently been presented and showed excellent effectiveness in limited research studies. In this study, a robust finite element (FE) model, featuring state-of-the art modelling techniques and nonlinear properties, is developed to study the flexural behaviour of reinforced concrete (RC) beams strengthened with S-NSM FRP bars. After validating its load, strain, and failure mode predictions with 6 full-size beam experiments, the model was used in an extensive parametric study on 108 new models, evaluating the effects of FRP bar diameter (d_f), strengthening length (SL), groove elevation (h_g), tensile steel reinforcement ratio (ρ_s), and concrete compressive strength ($f_c^{'}$). In general, the beam ultimate load (P_u) increased with SL, d_f, ρ_s, and $f_c^{'}$. The beam ductility also seems to be affected by the studied parameters but in general was satisfactory, averaging 2.30 to 2.73. A regression-based formula was presented for the effective FRP bar length, beyond which the brittle concrete peel-off failure is prevented, and P_u becomes constant. A sectional analysis was also performed coupled with regression, resulting in the development of a simple equation to calculate the FRP strain at beam failure and consequently an improved analytical model for predicting P_u.

1. Introduction

It is widely recognized that architecture, engineering, and construction (AEC) industry significantly impact the environment. Recently, several studies established strategies to reduce embodied carbon in buildings by utilization of low-carbon materials, material reuse, recycling, and minimal usage, selection of optimal structural systems and structural optimization, and optimization of construction operations [1–3]. In conjunction with these strategies in building and construction, various studies examined new effective materials to repair and strengthen existing structures to reduce CO2 emissions resulting from removing and establishing new buildings [4–6].

Fiber reinforced polymer (FRP) composites have become a mainstream method for repairing or retrofitting reinforced or prestressed concrete members, due to their high strength to weight ratio, noncorrosive nature, ease of handling and installation, and availability in many forms and shapes [7–9]. Two methods have been widely used to attach the FRP reinforcement when strengthening or repairing concrete work in bending, externally bonded (EB) system by adhesively bonding an FRP laminate or fabric to the member tension face, and near surface mounted (NSM) technique by cutting grooves/slits in the concrete cover and inserting FRP rods/strips, typically at the bottom face of a concrete member (B-NSM) [10,11]. When comparing the two, NSM method offers several advantages such as lower demands for surface preparation; better protection against environmental exposure and damage by fire, impact, and vandalism; higher debonding strains; easier to prestress or anchor; and more effective for strengthening negative moment regions of slabs and bridge decks [12–16].

Laboratory and field tests, in addition to numerical and analytical simulations, have confirmed the effectiveness of B-NSM FRP in strengthening concrete members deficient in shear [14,17], flexure [7,18], and torsion [19–21]. For example, the static and fatigue performances of RC beams were significantly enhanced when strengthened with un-prestressed and pre-stressed B-NSM carbon-FRP (CFRP) bars,

* Corresponding author.
E-mail address: akram.jawdhari@valpo.edu (A. Jawdhari).

https://doi.org/10.1016/j.istruc.2022.04.003
Received 20 January 2022; Received in revised form 31 March 2022; Accepted 1 April 2022
Available online 6 April 2022

Table 1
Reference beams details and key experimental and FE results.

Beam ID	FRP bar length (mm)	Filling materials	Bar elevation (mm) [1]	Failure load, P_u (kN)			Strain in CFRP	
				Exp.	FE	Exp./ FE	Exp.	FE
CB	—	—	—	72.8	71.2	1.02	0.0193	0.0191
BC1	2700	Epoxy	42	116.0	120.5	0.96	0.0082	0.0094
BC2	2100	Epoxy	42	106.4	103.7	1.03	0.0044	0.0055
BC3	2700	Mortar	42	106.0	107.6	0.99	0.0035	0.0037
BC4	2100	Mortar	42	94.1	94.1	1.00	0.0033	0.0030
BC5	2700	Epoxy	62	102.7	109.2	0.94	0.0104	0.0093

[1] Elevation is taken as the distance from the centroid of the FRP bar to the concrete bottom face.

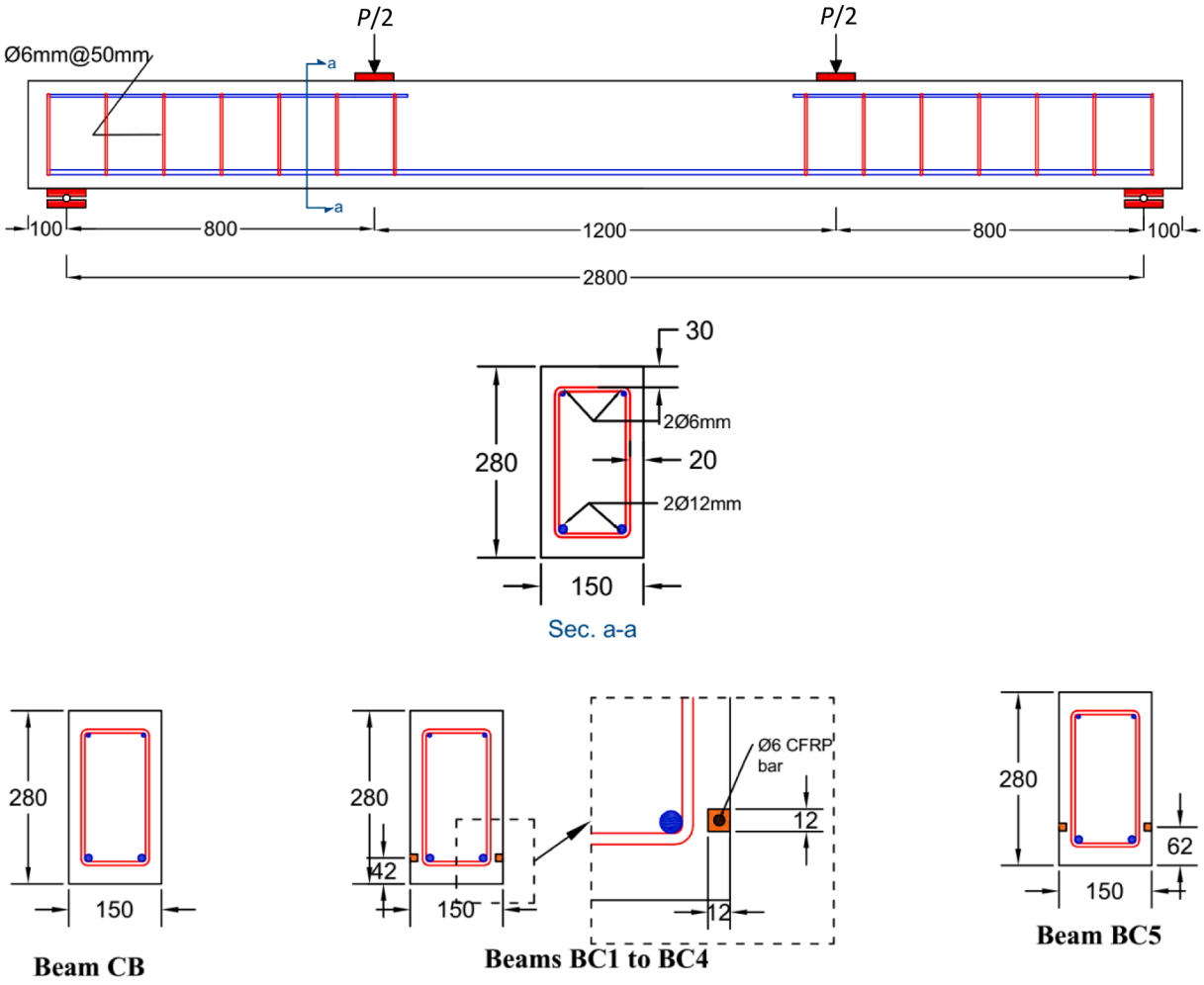

Fig. 1. Reinforcement details and strengthening configurations, for reference beams in [27].

with the ultimate load increasing by 50 to 79% [22]. Foret and Limam 2008 [23] tests also showed a significant increase in strength and stiffness of two-way RC slabs strengthened with NSM FRP rods. Kadhim et al. [14] developed a numerical model for reinforced concrete (RC) beams strengthened in shear with NSM CFRP bars and investigated the effects of concrete strength, NSM and internal steel reinforcement ratios, and distance between NSM bars and steel stirrups. Lap-splicing of NSM bars, which is an important issue when strengthening long span members, was also studied and recommendations for the optimum splice length and configuration were given in [10]. Abdallah et al. [7] extended the application of NSM FRP system into statically indeterminate members and tested 6 two-span continuous RC beams, varying NSM reinforcement ratio, length of NSM bars in the sagging and hogging regions, and adhesive material.

However, B-NSM technique has several practical drawbacks that limit its full potential; for example, to avoid premature debonding failure due to stress overlapping, the member soffit must have a sufficient width to accommodate multiple NSM bars and meet minimum code limits for groove-to-groove spacing and edge distance [24]. In some cases, available width can't accommodate more than one NSM bar, such as narrow double-T beams. In other scenarios, the beam soffit is occupied or inaccessible due to presence of wall partitions, utility services such as suspended ceilings, air ducts, and electrical wiring [25]. The system is also prone to concrete peeling-off failure where cracks typically form at the termination point for the NSM bar(s) and progress toward the tensile steel reinforcement, causing detachment of the concrete cover [15,24,26]. Some research has shown that the debonding and peeling-off failures can be mitigated with the use of end anchorage

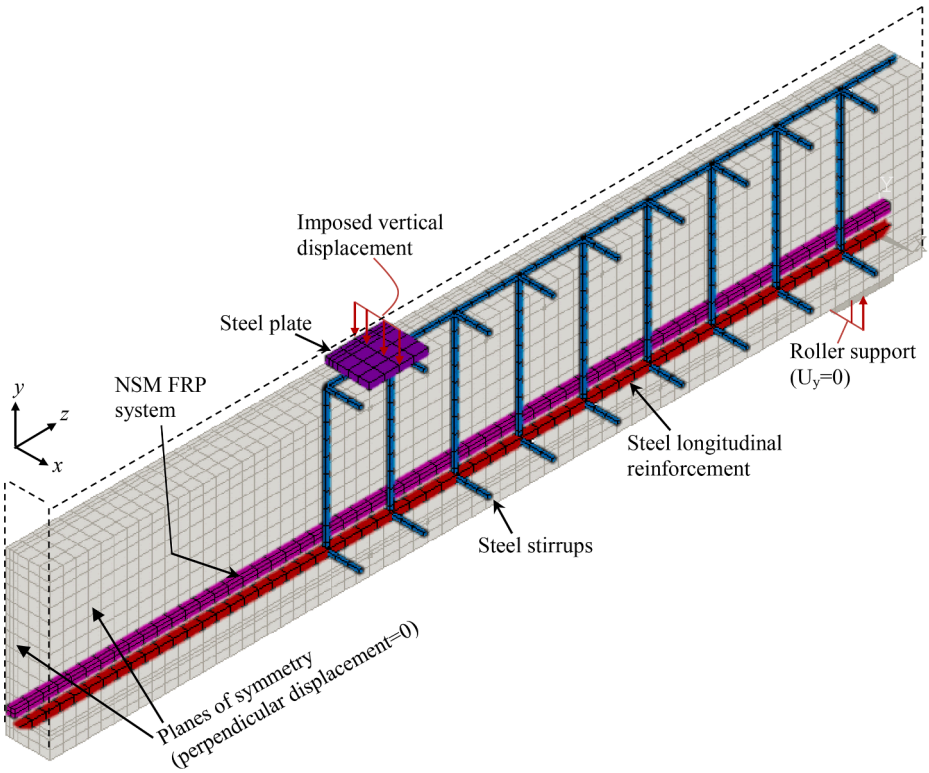

Fig. 2. Typical quarter-size FE model for RC beams strengthened with SNSM FRP bars.

bars, U-wraps, or 45° or 90° hooked-end NSM bars [27].

A simple solution to above concerns, used first for EB FRP system [28,29] and recently extended for NSM technique, is by applying the NSM bars at the beam sides (S-NSM). Hosen et al. [13] tested several RC beams strengthened with S-NSM CFRP bars and found the system to increase the beam yield and ultimate load capacities by 2 and 2.83 times, respectively. In another study, CFRP strips were utilized for the S-NSM technique instead of rods and were shown to increase the ductility, stiffness, and energy absorption capacity of strengthened beams [12]. Shukri et al. [30] showed that the system results in a marginally smaller ultimate capacity than B-NSM but yields a higher stiffness if it is used to strengthen pre-cracked RC beams instead of virgin (un-cracked) samples. Glass-FRP (GFRP) bars have been utilized for S-NSM FRP system in two studies [31] and were shown to be as effective as CFRP counterparts. Sabau et al. [15] compared S-NSM and B-NSM systems and found the former to be successful in avoiding concrete peeling-off with increased beam rotational capacity and energy dissipation at failure. Haddad and Yagmour [32] examined trapezoidal and parabolic profiles to improve S-NSM resistance to brittle failures.

Because it is relatively new, S-NSM FRP system has not received as much attention as B-NSM FRP or EB FRP techniques, and several research gaps are still to be studied before it can be adopted for wide use. For example, no finite element (FE) articles could be found on the topic. Also, multiple key parameters that might affect the system performance and that of the strengthened member are yet to be examined. Of these, NSM bar length and its elevation relative to the beam soffit correlate with concrete peel-off and debonding failures and thus affect the strength and ductility of strengthened member. In this study, a robust three-dimensional FE model has been developed for RC beams strengthened in flexure with S-NSM FRP bars, featuring state-of-the art modeling techniques such as adopting nonlinear material properties and simulating FRP slipping and debonding failures. After validation, the model was used in an extensive parametric study, examining multiple governing variables. Results from the parametric study were also compared with an existing analytical model and a new formula was developed from regression and presented for the maximum strain in FRP bar at failure, which is then used to calculate the ultimate capacity of RC beams strengthened with S-NSM FRP bars.

2. Experimental reference

RC beams tested by Abdallah, Al Mahmoud [33], were chosen in this study to calibrate and validate the accuracy of the presented FE model. The experimental program consisted of six beams, one of them was without strengthening (control), and five specimens were strengthened with S-NSM CFRP bars, having two bar lengths of 210 and 270 mm (or 0.75 and 0.94 of span), two filling adhesives (epoxy or mortar), and two CFRP bar elevations of 42 and 62 mm, Table 1. The beams were tested under four-point bending to failure, had dimensions of 150 × 280 × 2800 (width × depth × span), and were reinforced with 2Ø12 mm and 2Ø 6 mm tensile and compressive steel rebars, respectively, Fig. 1. They were designed to fail in flexure, thus were over reinforced in shear with Ø6 mm stirrups spaced at 150 mm, covering the entire shear span, Fig. 1. For the strengthened samples, two Ø 6 mm CFRP bars, one in each side of the beam, were used as S-NSM reinforcement and were installed inside 12x12 mm grooves cut in the side cover with a special concrete saw, Fig. 1.

The concrete properties, determined from material testing reported in the study, were 37 MPa for the 28-compressive strength (f_c`), 3.0 MPa for the tensile strength (f_t), and 30.3 GPa for the elastic modulus (E_c). In addition, the yield strength, and the modulus of elasticity of steel reinforcement were also tested and reported to be 600 MPa and 210 GPa, respectively. The tensile strength and Young's modulus for the CFRP bars were 1875 MPa and 146 GPa, respectively [27]. The beams were instrumented with load cell to record load, linear variable differential transducer (LVDT) to measure deflections, and foil-type strain gages to measure CFRP and steel rebar strains at mid-span. The study by Abdallah, Al Mahmoud [33] reported a wealth of information to validate the FE model results, including load–deflection, and load- CFRP (or steel) strain curves, and photos of failure modes.

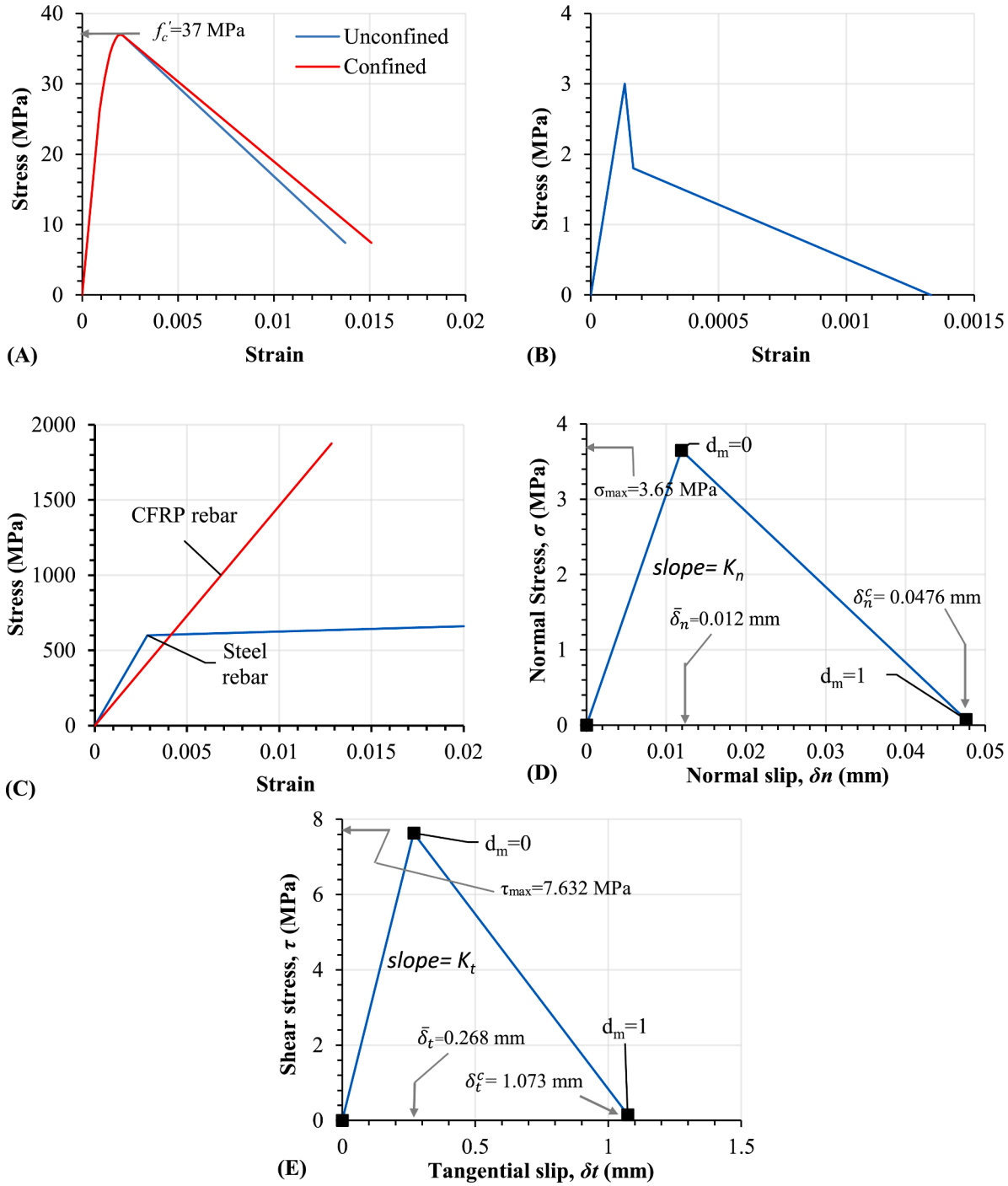

Fig. 3. Constitutive models for: (A) concrete in compression, (B) concrete in tension; (C) steel and CFRP bars; (D) bilinear normal stress-slip, and (E) bilinear shear stress-slip models.

Table 2
Bond-slip model inputs for CONTA 173 elements.

Property	Definition	Unit	Value
τ_{max}	Maximum contact shear stress	MPa	7.632
G_{ct}	Shear fracture energy	N/mm	4.096
σ_{max}	Maximum normal contact stress	MPa	3.650
G_{cn}	Normal fracture energy	N/mm	0.087
η	Artificial damping coefficient	—	0.001

3. FE model development

The commercial FE software ANSYS APDL 17.2 [34] was used to develop the numerical models for the RC beams strengthened with S-NSM CFRP rebars. To minimize computational efforts and computer desk space, a quarter-size model was adopted for all validation and parametric study simulations. Fig. 2 shows a schematic of a typical quarter-size beam FE model, showing the model different components. The load was applied as displacement to simulate a displacement-controlled loading which is more stable than force-controlled one and capable of predicting the post-peak and brittle failure modes [35]. Proper displacement restraints were applied at the planes of symmetry

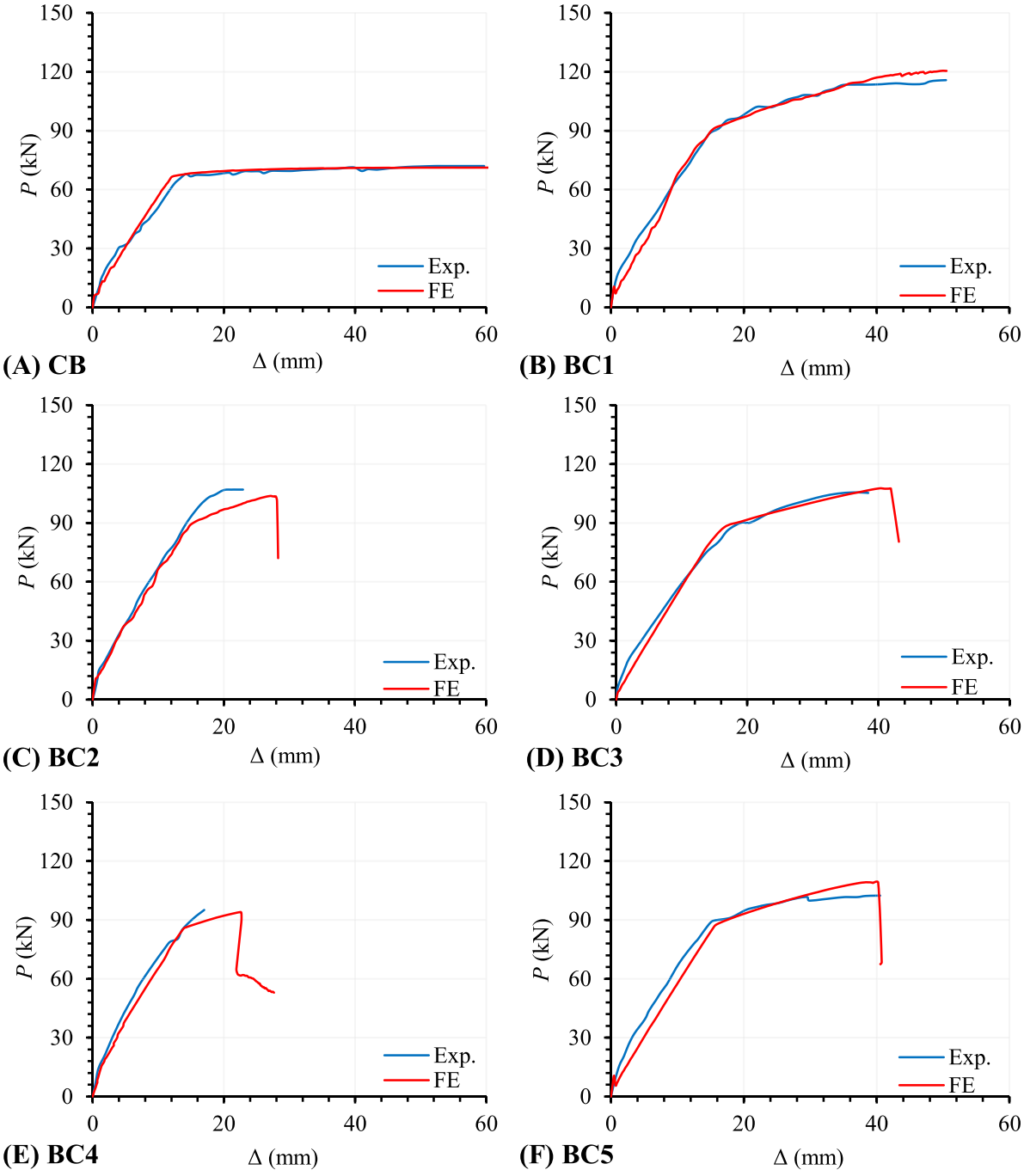

Fig. 4. Comparison of load (*P*) vs. mid-span deflection (Δ) curves obtained from experimental and FE results.

representing the quarter-size representation, Fig. 2. A mesh sensitivity analysis on the control (un-strengthened) beam showed that using a 25 mm element size for concrete and other parts can result in a good balance between solution accuracy and computational efforts. The Newton-Raphson integration method, with automatic load bisection and iteration, was activated to solve the highly nonlinear behaviour, while a force criterion of 5% was selected for convergence. Both material and geometric nonlinearities were considered, providing an accurate simulation of possible failure modes such as crushing and cracking in concrete, debonding and rupture of S-NSM CFRP reinforcement. The following subsections discuss the modelling procedure undertaken in this analysis.

3.1. Element types

Brick element "SOLID65", with 8 nodes and three degrees of freedom (DOF) per node along with special features for modelling concrete cracking and crushing, were used to represent the concrete beams. Similar 8-noded "SOLID185" element was used for the filling adhesives and steel plates that were added at loading and support regions to minimize stress concentrations and local failure. A two-node truss type element "LINK180" was used to model the steel and CFRP rebars and shear stirrups. A perfect-bond condition was assumed for the surface between steel bars/stirrups and concrete and was modelled by the "merge node" option. A contact-target pair, comprising "CONTA173" and "TARGE170" elements, was used to simulate the interface between

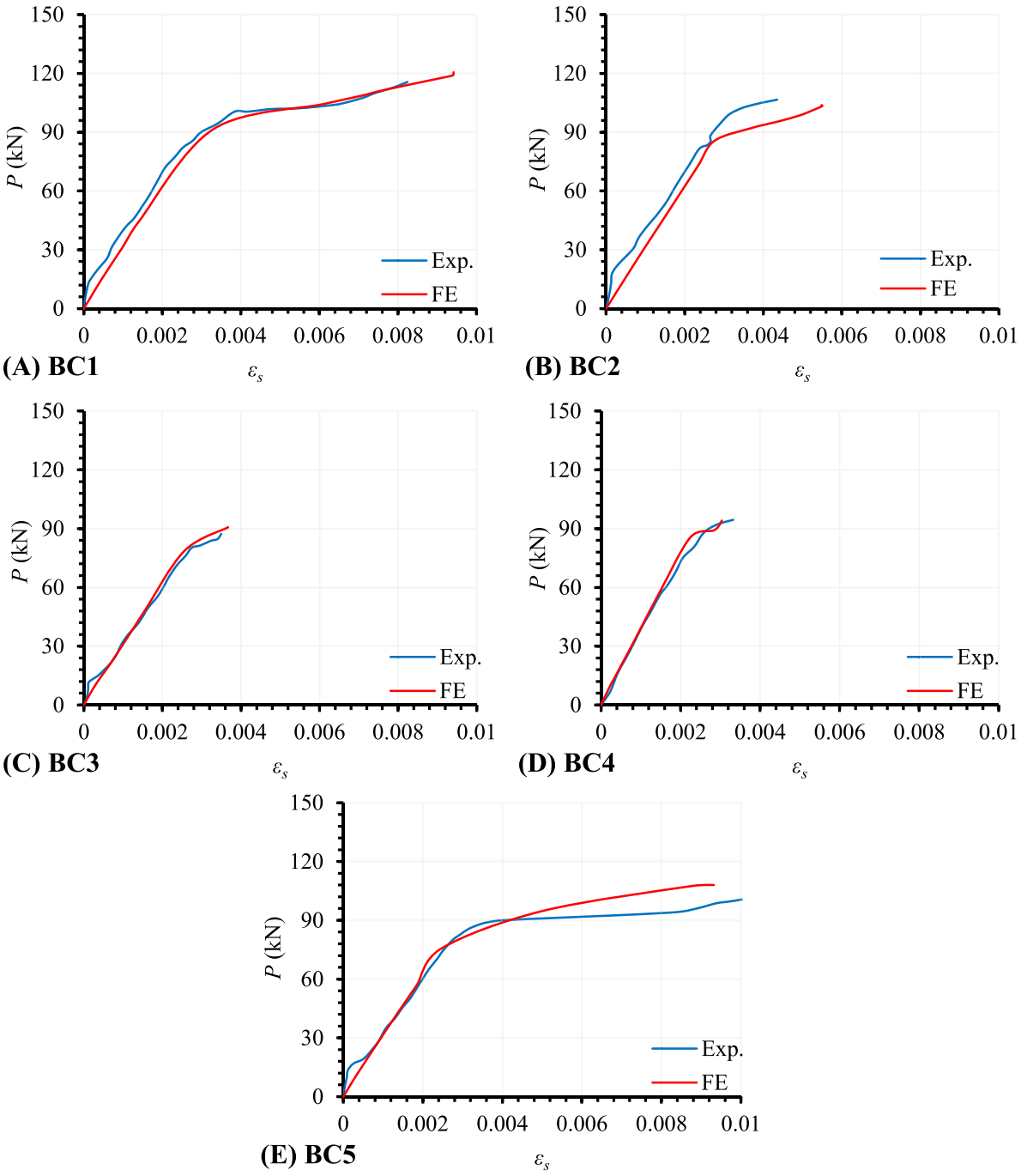

Fig. 5. Comparisons of experimental and FE results, curves of load (P) versus strain (ε_s) in steel bars.

concrete and filling adhesive for S-NSM reinforcement, which could also experience slipping and debonding failure as observed in multiple studies [14,17,19]. When defining the contact-target pair, and following ANSYS [34] recommendations, the concrete surface was selected as the target surface and the adhesive as contact. A bond-slip relation is required for the contact-target pair and will be discussed in Section 3.3.

3.2. Material properties

3.2.1. Concrete

the plasticity model available in ANSYS, based on William and Warnke [36] failure criteria, is used to model the concrete beams because of its ability to simulate cracking and crushing failures, compressive nonlinear behaviour, tension and shear softening across the crack face [14]. Kent and Park [37] model is adopted to represent the concrete stress–strain curve in compression and is shown graphically in Fig. 3(a) for a concrete with $f_c^{'}$=37 MPa. The model consists of a linear portion till a stress (f_c) of $0.45f_c^{'}$, a non-linear upward curve until reaching $f_c^{'}$, and a linear descending line afterword continuing until a stress of $0.2f_c^{'}$, Fig. 3 (a). Concrete confinement due to shear stirrups is incorporated in the model within the slope of the post-peak line [37], as a function of the stirrups size and spacing. In particular, the concrete volume was divided into regions, (1) an unconfined one comprising the hollow concrete box outside of the stirrups and the entire concrete part within the constant moment region where stirrups are not used, and (2) a confined region representing the inner concrete core within the shear

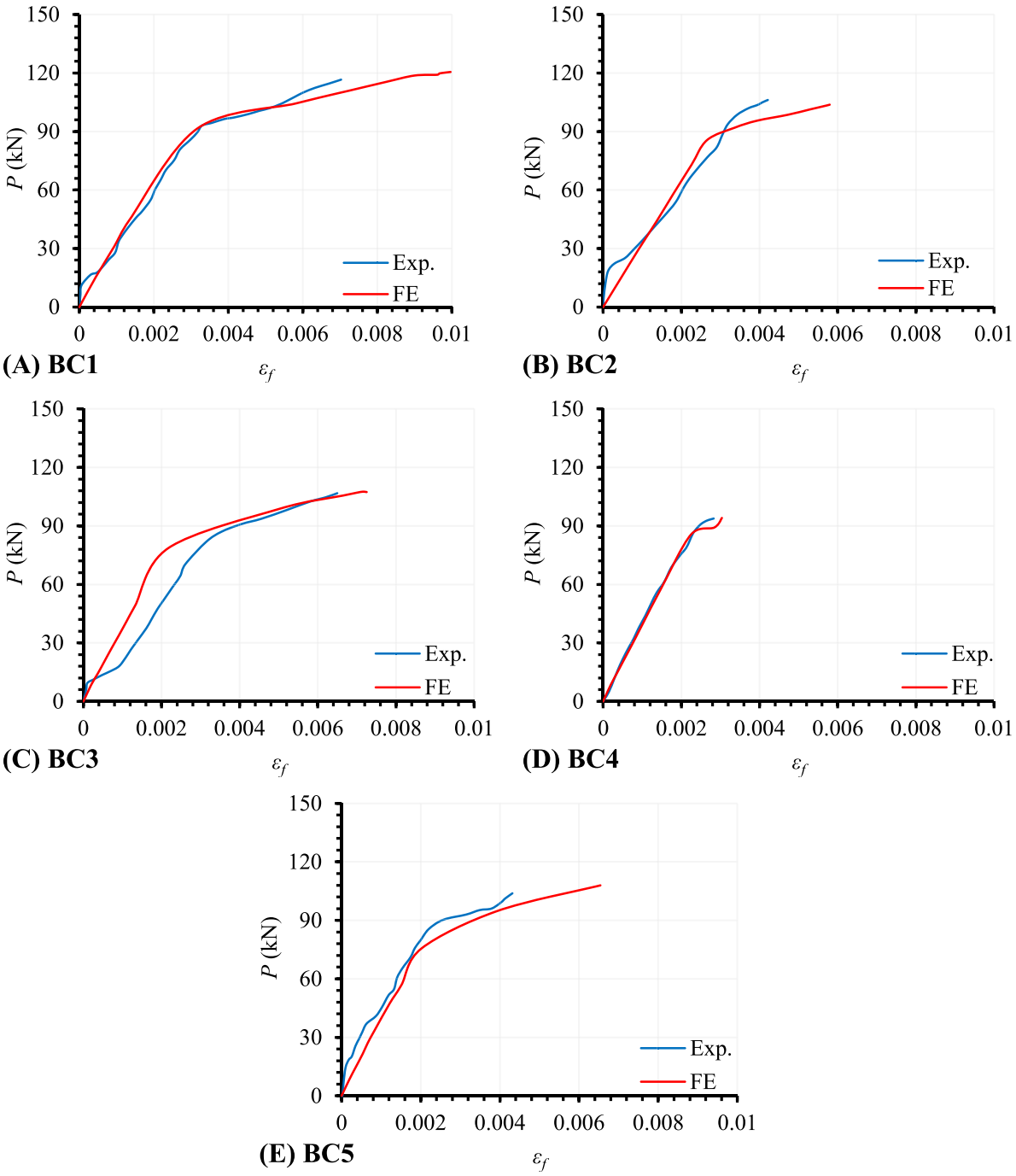

Fig. 6. Comparisons of experimental and FE results, curves of load (P) versus strain (ε_f) in NSM CFRP bars.

span where shear stirrups are present. As shown in Fig. 3 (a), the stress–strain curve for confined concrete is more ductile (its ultimate strain is larger than that for unconfined concrete), and the ductility of the former depends on the size and spacing for shear stirrups [31]. The mathematical formulation for Kent and Park model, including the effects of confinement, can be viewed in the authors' previous work [14,38] and are not repeated here for conciseness. The concrete is assumed to behave linearly in tension until reaching the cracking strength (f_t), followed by a drop to a stress of 0.6 f_t, with a gradual reduction afterward to an eventual zero stress at a strain of 6 times that at f_t, Fig. 3 (b). It should be noticed that while the values reported in [27] were used for f_c', f_t, and E_c for the beams with f_c'=37 MPa, the equations from the American Concrete Code (ACI 318-19 [39]) of $f_t = 0.625\sqrt{f_c'}$ and $E_c = 4700\sqrt{f_c'}$, were used to obtain numerical values for f_t and E_c when other concrete strengths were used in the parametric study. The concrete Poison's ratio (v_c) was assumed to be 0.18 [40,41]. The open (β_o) and closed (β_c) shear coefficients are needed to define the residual shear force transferred in a cracked concrete and were assumed to be 0.2 and 0.8, respectively [40,41].

3.2.2. Steel

the steel reinforcement was modelled as an elastic-perfectly plastic material as shown in Fig. 3 (C), using the yield stress and elastic modulus values reported in Section 2 and a Poison's ratio (v_s) of 0.3 [42]. A similar model was used for the steel plates at loading and support

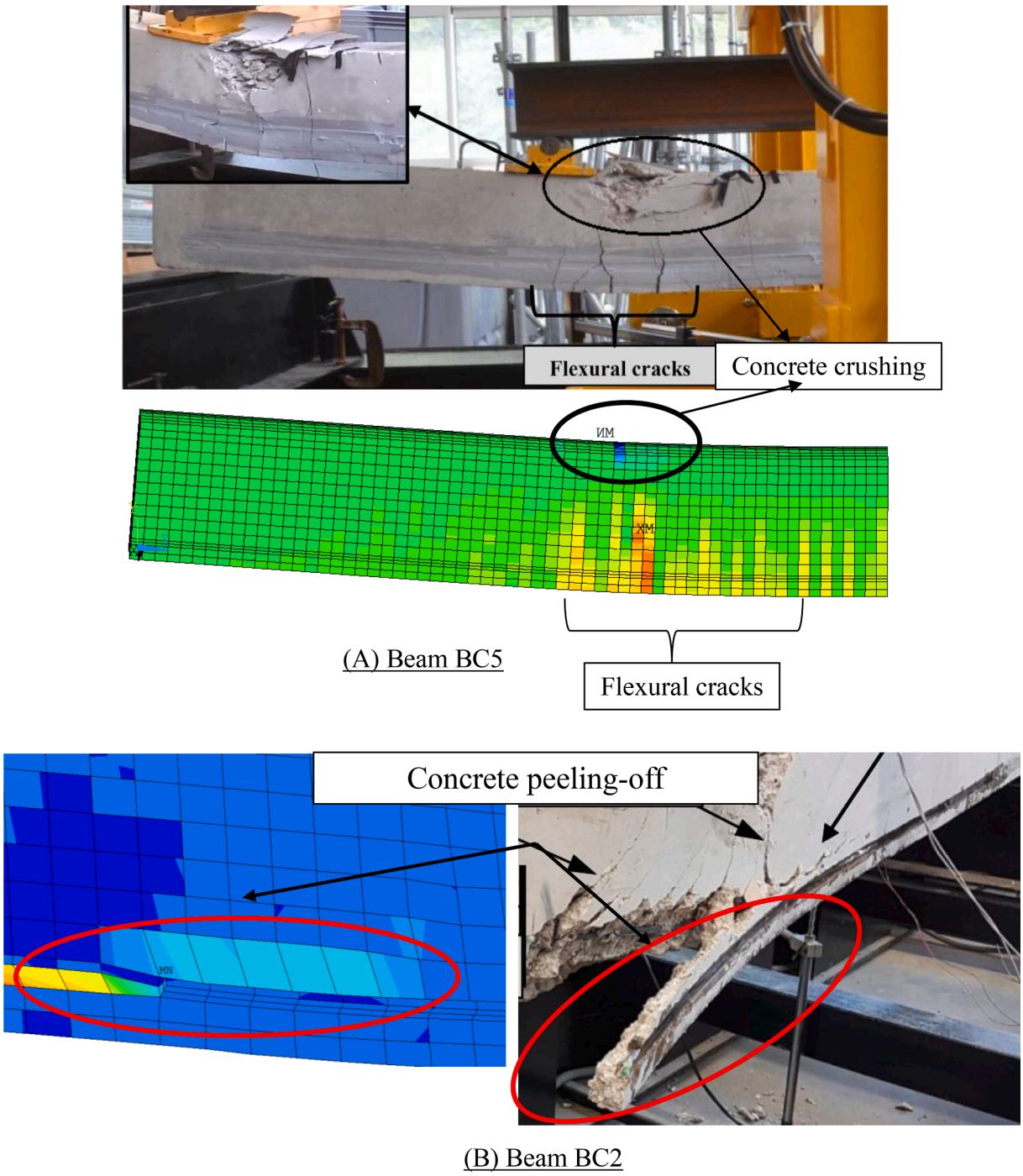

Fig. 7. Comparisons of failure modes from experimental and FE results.

locations but without the yielding option.

3.2.3. CFRP & adhesive

a linear elastic material model (Fig. 3 (c)) was used for the CFRP bars and the filling adhesives, using the material properties reported in [27] for each part. A yeilding creteria, similar to that defined in Section 3.2.2 for steel, was added for the CFRP bars to track the potential rupture failure, in which the yiedlnig stress was assumed to be the tensile strength of CFRP. This was done because the conventional composite damage models for FRP in ANSYS are formulated for shell and solid elements, and are not applicable for axial members (e.g. trusses, rods). A Poison's ratio (v_f) of 0.3, (v_a) of 0.35, and (v_c) of 0.18 was assumed for CFRP rebar, epoxy adhesive, and mortar, respectively [40,41].

3.3. Interface modelling

As mentioned in Section 3.3, both the spring element and contact-target pair require an interfacial relationship to define slipping and debonding failures of NSM FRP bars. For the contact-target pair defined at the adhesive-concrete interface, a mixed-mode debonding model where both tangential (shear) and normal (peeling) stresses contribute to the debonding failure was adopted due to the effects of beam curvature [43]. The following inputs define the debonding model: maximum normal stress (σ_{max}), maximum shear stress (τ_{max}), normal fracture energy (G_{cn}), and shear fracture energy (G_{ct}). These inputs are utilized in ANSYS as bilinear bond-slip curves relating the normal (σ) or shear (τ) stresses with normal (δ_n) or tangential (δ_t) slips, as can be seen

Table 3
Ductility index (μ) for beams with various reinforcement ratios.

SL (mm)	df (mm)	h_g (mm)	h_g/h	Ductility (μ)	
				ρs=0.0062	ρs=0.0027
800	6	42	0.13	2.74	3.72
660	6	42	0.13	2.98	3.65
520	6	42	0.13	2.74	3.28
380	6	42	0.13	2.10	2.13
800	8	42	0.13	2.07	3.09
660	8	42	0.13	1.82	2.83
520	8	42	0.13	1.60	1.97
380	8	42	0.13	1.17	1.44
800	10	42	0.13	1.79	2.34
660	10	42	0.13	1.64	1.95
520	10	42	0.13	1.30	1.38
380	10	42	0.13	1.08	1.16
800	6	62	0.20	3.52	4.12
660	6	62	0.20	3.40	4.25
520	6	62	0.20	3.55	3.89
380	6	62	0.20	2.94	2.65
240	6	62	0.20	2.21	2.15
800	8	62	0.20	2.54	3.68
660	8	62	0.20	2.71	3.34
520	8	62	0.20	2.33	2.52
380	8	62	0.20	1.90	1.83
240	8	62	0.20	1.27	1.57
800	10	62	0.20	2.11	2.82
660	10	62	0.20	1.95	2.46
520	10	62	0.20	1.61	1.79
380	10	62	0.20	1.44	1.38
240	10	62	0.20	1.28	1.78
800	6	82	0.27	3.50	4.76
660	6	82	0.27	3.42	4.71
520	6	82	0.27	3.65	4.73
380	6	82	0.27	3.35	3.22
240	6	82	0.27	2.18	2.17
800	8	82	0.27	2.68	3.89
660	8	82	0.27	2.98	3.70
520	8	82	0.27	2.87	3.30
380	8	82	0.27	2.28	2.11
240	8	82	0.27	1.77	1.58
800	10	82	0.27	2.45	3.14
660	10	82	0.27	2.40	3.12
520	10	82	0.27	2.12	2.20
380	10	82	0.27	1.62	1.63
240	10	82	0.27	1.42	1.40

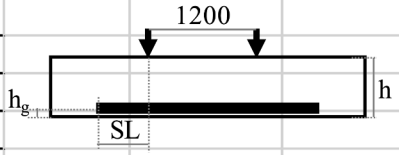

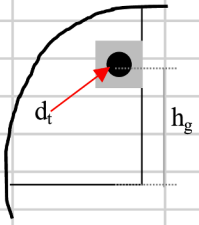

SL: strengthening length of FRP bars
h_g: grooves height
h: total beam height
d_f: diameter of FRP bars
μ: ductility of beams

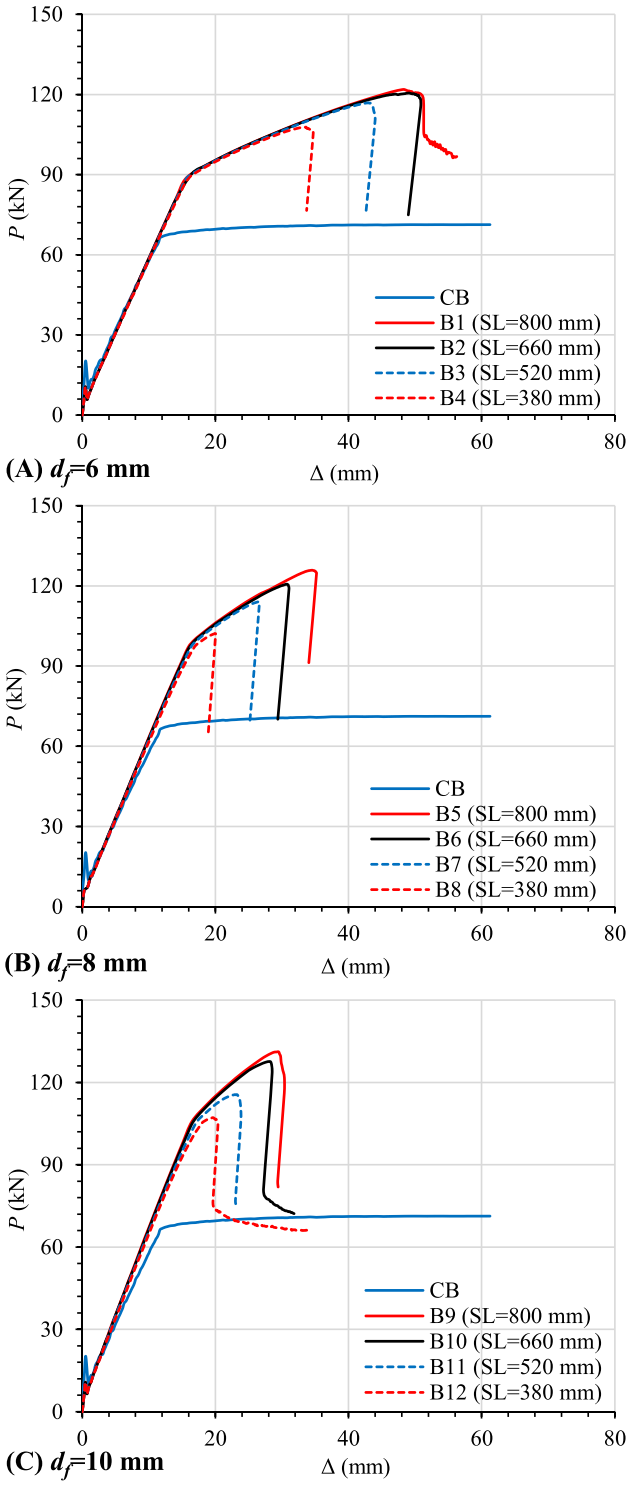

Fig. 8. Load (P) vs. mid-span deflection (Δ) for beams with grooves heights (h_g) = 42 mm and various FRP bar diameters (d_f) and lengths (SL).

in Fig. 3 (d, e). It can be seen from this figure that debonding in either the normal or tangential directions starts when the damage parameter $d_m = 0$ and ends when $d_m = 1$. The following equations define the relations between σ (or τ) and δ_n (or δ_t):

$$\tau_t = K_t\delta_t(1 - d_m) \tag{1}$$

$$\sigma_n = K_n\delta_n(1 - d_m) \tag{2}$$

where K_n and K_t are the normal and tangential contact stiffnesses respectively, and d_m is calculated from Eq. (3):

$$d_m = \left(\frac{\Delta_m - 1}{\Delta_m}\right)\chi \tag{3}$$

with Δ_m and χ parameters defined as:

$$\Delta_m = \sqrt{\left(\frac{\delta_n}{\overline{\delta}_n}\right) + \left(\frac{\delta_t}{\overline{\delta}_t}\right)} \tag{4}$$

$$\chi = \frac{\delta_n^c}{\delta_n^c - \overline{\delta}_n} = \frac{\delta_t^c}{\delta_t^c - \overline{\delta}_t} \tag{5}$$

where $\overline{\delta}_n$ and $\overline{\delta}_t$ are the normal and tangential slips accompanying σ_{max} and τ_{max}, respectively, δ_n^c and δ_t^c are normal and tangential slips at complete debonding, respectively. In this study, $\overline{\delta}_n$ and $\overline{\delta}_t$ are assumed to be 25% of the respective δ_n^c and δ_t^c slips.

The formulation developed by Seracino et al. [44] is adopted in this study to determine the above interfacial inputs required for the mixed-mode debonding model, using the following equations:

$$\tau_{max} = (0.802 + 0.078\varphi)f_c^{'0.6} \tag{6}$$

$$G_{ct} = \frac{0.976\varphi^{0.526}f_c^{'0.6}}{2} \tag{7}$$

where φ is the interface aspect and can be calculated from Eq. (8) as a function of the groove dimensions:

$$\varphi = \frac{Groove\ depth + 1\ mm}{Groove\ width + 2\ mm} \tag{8}$$

In addition, given that peeling failure oftentimes occurs in a thin layer within the concrete member, σ_{max} was assumed equal to f_t. The normal fracture energy (G_{cn}) is determined from CEB-FIB code [45] as follows:

$$G_{cn} = G_{fo}\left(\frac{f_c^{'}}{10}\right)^{0.7} \tag{9}$$

The fracture energies, G_{cn} and G_{ct}, represent the area under the stress-slip curves and thus can be used to determine the slips (δ_n^c, δ_t^c) at complete debonding, according to the following equations:

$$G_{ct} = 0.5\tau_{max}\delta_c^t \tag{10}$$

$$G_{cn} = 0.5\sigma_{max}\delta_c^n \tag{11}$$

Table 2 lists the numerical values for the interfacial inputs, applicable only for the validation models with an $f_c^{'}$=37 MPa. When using other concrete strengths in the parametric study, Eqs. (6) to (11) were repeated to produce new interfacial inputs. In Table 2, artificial damping coefficient (η) is introduced to overcome convergence difficulties that are typical with debonding problems [34]. The shear stress-slip (τ - δ_t) relation defined earlier and shown in Fig. 3 (d) was also used for the spring element, but the stress was converted into a force based on CFRP bar diameter, resulting in a force-slip model. A command subroutine was used to introduce the interfacial inputs into ANSYS environment given that the contact model is not readily available in the graphical user interface setting.

4. Validation of FE model

The six beams tested by [27] were simulated numerically and used to illustrate the validity and accuracy of the proposed FE model in reproducing the behaviour of RC beams strengthened with S-NSM FRP reinforcement. The FE versus experiments comparisons included the percentage difference in ultimate load (P_u), load vs. mid-span deflection

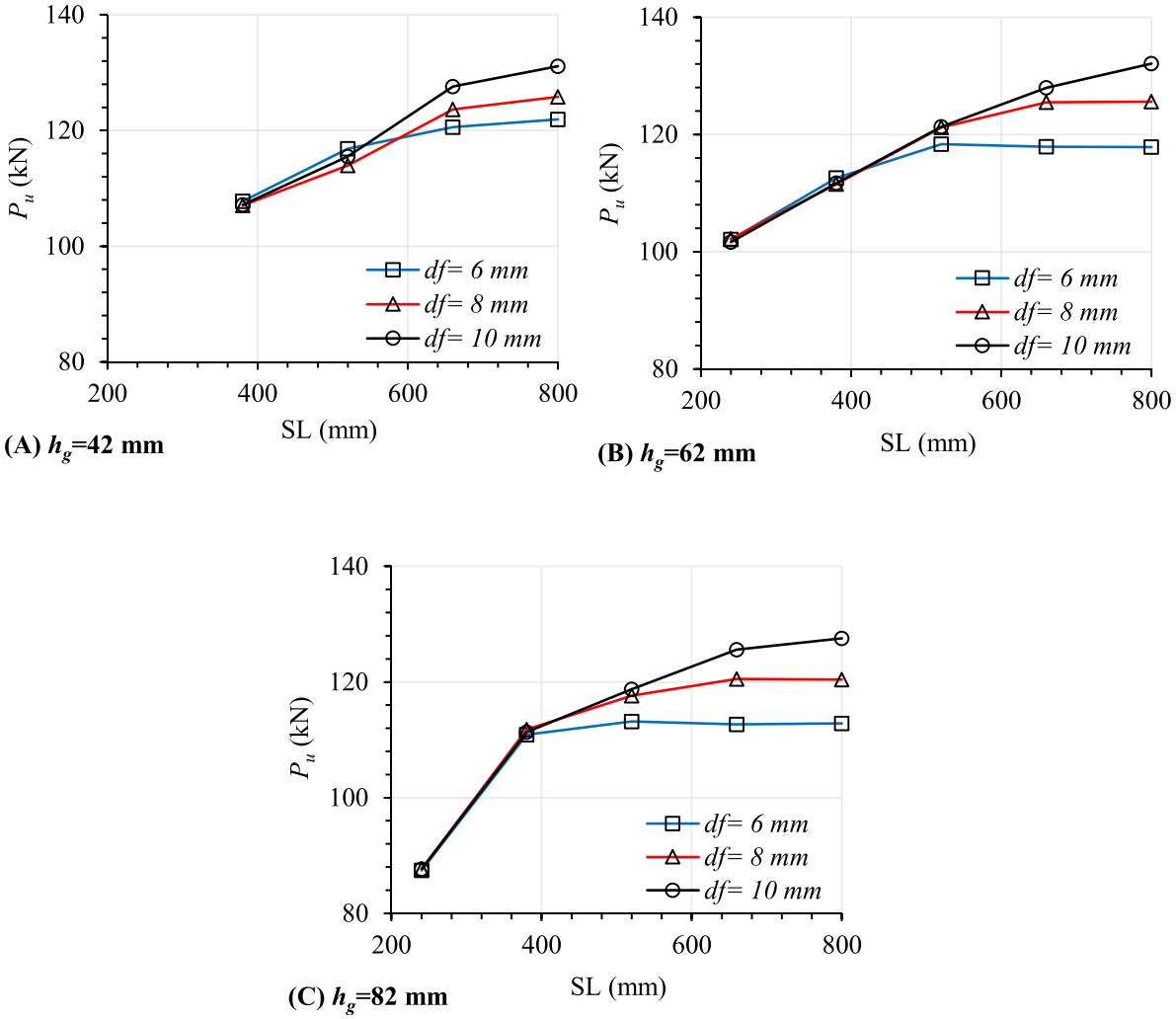

Fig. 9. Ultimate load (P_u) vs. strengthening length (SL) comparisons for various FRP bar diameters (d_f) and grooves heights (h_g).

(P-Δ) curves, load vs. steel rebar strain (P-ε_s) curves, load vs. CFRP rebar strain (P-ε_f) curves, and failure modes. Table 1 lists P_u from testing and FE simulation, for each of the 6 beams, and shows that the percentage of experimental-to-FE based P_u ranged between 0.94 and 1.03,with an average of 0.99 for all, reflecting the model robustness in capturing the beam capacity.

Fig. 4 plots the experimental and numerical P-Δ curves for all beams and shows how the model was able to replicate the entire load–deflection behaviour and capture various milestones within the curves, such as loads at cracking and steel yielding, stiffness at pre- and post-cracking and post-yield stages, and deflections at ultimate load. The curves for strengthened beams show a mostly bilinear response, with the slope and extension of second line dependent on the length and elevation of NSM bars. Fig. 5 plots the experimental and numerical P-ε_s where (ε_s) is measured in the tensile rebar at mid-span. A similar plot is shown in Fig. 6 for P-ε_f curves, using the CFRP bar at mid-span also. The figures show clearly that there is a good agreement between the measured and predicted strain values for the steel and CFRP reinforcements in all simulated beams.

In the experiments of Abdallah, Al Mahmoud [33], three governing failure modes were reported; concrete crushing near one of the loading points preceded by yielding of tensile steel and excessive concrete cracking in the tensile zone for beams CB, BC1, and BC5; slipping and partial debonding of CFRP bar for beams with mortar as the filling adhesive (beams BC3 and BC4); and concrete peeling-off failure for beam BC2 with a CFRP bar length of 2100 mm. Fig. 7 shows photos of observed failure modes from testing and analogous FE stress contours and deformed shape, for two representative specimens (BC2 and BC5). The figures shows that the model can simulate several failure modes, particularly the brittle concrete peel-off. Hence, it can be concluded that the proposed FE model is able to capture the performance of RC beams bonded to S-NSM FRP technique and can be used in an exploratory parametric analysis of several key variables that have not been investigated previously or studied with limited range and scope.

5. Parametric study

The validated FE model is used in this section to conduct a parametric study into the effects of key variables affecting the behaviour of S-NSM FRP strengthened RC beams, namely: FRP bar diameter (d_f) and strengthening length (SL), where SL is measured from the bar termination point to the nearest loading point as shown in Table 3; groove elevation (h_g) relative to beam soffit; tensile steel reinforcement ratio (ρ_s), and concrete compressive strength (f_c'). The following sub-sections discuss the results for the studied variable.

5.1. Effects of d_f, SL, and h_g

Three FRP bar diameters (d_f) were investigated in this study, 6, 8, and 10 mm in combination with three groove elevations (h_g), 42, 62, and 82 mm, and five strengthening lengths (SL) of 240 (occasional), 380, 520, 660, and 800 mm. In total, 42 S-NSM FRP strengthened RC beam

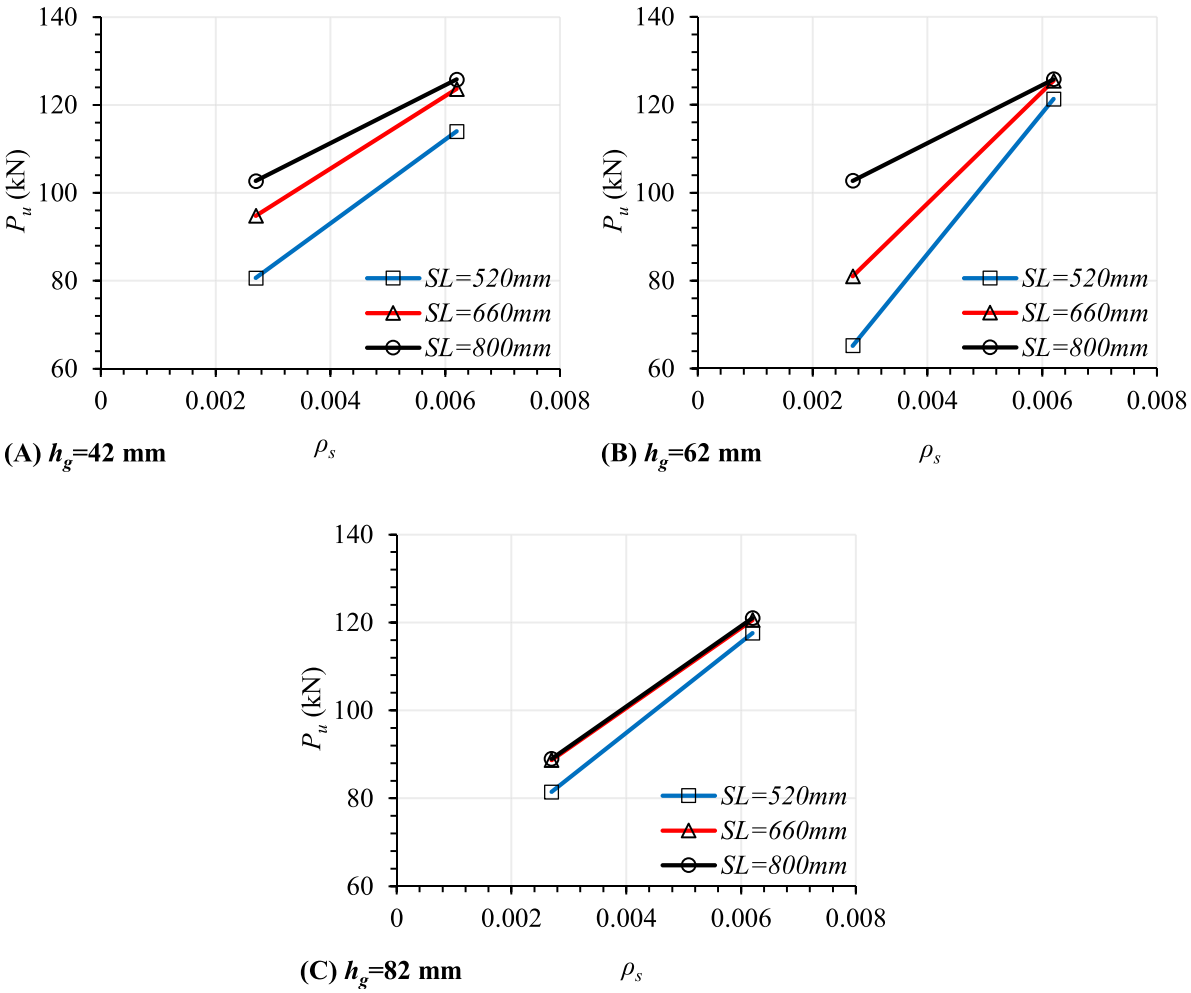

Fig. 10. Ultimate load (P_u) vs. steel reinf. ratio (ρ_s) for various strengthening lengths (SL) and grooves heights (h_g), and bar diameter d_f = 8 mm.

models were created in this section. Fig. 8 plots the (P-Δ) curves for beams with various d_f and SL values and an h_g = 42 mm. It can be seen from this figure that increasing d_f results in a systematic increase in the beam yielding and ultimate loads, but an un-significant increase in stiffness. Increasing SL for each d_f results in a consistent and significant increase in ultimate load and ductility. For example, P_u increased by 23% when SL increased from 380 to 800 mm. The increase in P_u of strengthened models relative to the control (un-strengthened) beam ranged between 44 and 82% and is a function of d_f and SL. The failure mode was yielding of tensile steel reinforcement followed by concrete crushing for beams with $SL > SL_{eff}$, and concrete peel-off for $SL < SL_{eff}$ values. The minimum SL length that evades the peel-off failure is of a particular importance to the S-NSM FRP system and hereinafter will be referred to as the effective FRP length (SL_{eff}).

Fig. 9 plots the relation between P_u and SL for the strengthened beams with various d_f, and h_g values. For each h_g, the effects of d_f on P_u seem negligible for short SL values but increase as SL increases, particularly for SL>520 mm. For example, at SL = 800 mm, P_u increased by 7.5%, 12.1%, and 13.0%, for h_g = 52, 62, and 82 mm, respectively, as d_f increased from 6 to 10 mm. From Fig. 9 and observing that once the concrete peel-off failure is avoided, beams bonded to S-NSM FRP bars with equal d_f and h_g would theoretically have an identical P_u regardless of bar length (SL). Hence, the effective length (SL_{eff}) can be estimated as the length beyond which P_u plateaus. SL_{eff} can be easily extracted from Fig. 9 for several cases (e.g., SL_{eff} = 520 mm for d_f = 6 mm and h_g = 62 mm) but in others it is difficult to determine because concrete peel-off failure was still appearing in tandem with concrete crushing and P_u was still increasing. SL_{eff} is affected greatly by h_g where the larger the groove elevation is the more SL_{eff} becoming clear to determine from Fig. 9. This is because increasing h_g reduces the likelihood of concrete peel-off failure where higher embedment elevations offer better confinement for the FRP bar and less stress concentrations at bar ends [24]. The benefits of increasing h_g related to the peel-off failure seem to outweigh the expected decrease in P_u associated with the reduction in the moment arm as h_g increases. For example, at SL = 800 mm and d_f = 10 mm, P_u only reduced by 2.7% when h_g increased by 95% (from 42 to 82 mm).

5.2. Effects of ρ_s

In addition to the original tensile steel reinforcement ratio (ρ_s) of 0.0062 that is used in the reference experiments by [27] and in the previous section, two ρ_s ratios are examined in this section, 0.0027 and 0.011, representing the minimum and maximum ratios determined according to ACI 318-19 [39]. Effects of ρ_s = 0.011 are not discussed further since it resulted in a change of failure mode to shear due to over reinforcing the beam in flexure when combining effects of steel and FRP bars. Using ρ_s of 0.0027, 42 new beam models were created, and their results compared with those with ρ_s = 0.0062. Fig. 10 plots the relation between P_u and ρ_s for a bar diameter d_f of 8 mm and various SL and h_g values. Increasing ρ_s 2.3 times from 0.0027 to 0.0062 resulted in an average (for all SL values) increase in P_u by 31.4, 58.9, and 38.7% for h_g = 42, 62, and 82 mm, respectively. A similar plot to Fig. 9 (P_u vs. SL for different h_g) was also constructed for ρ_s = 0.0027 but not presented to

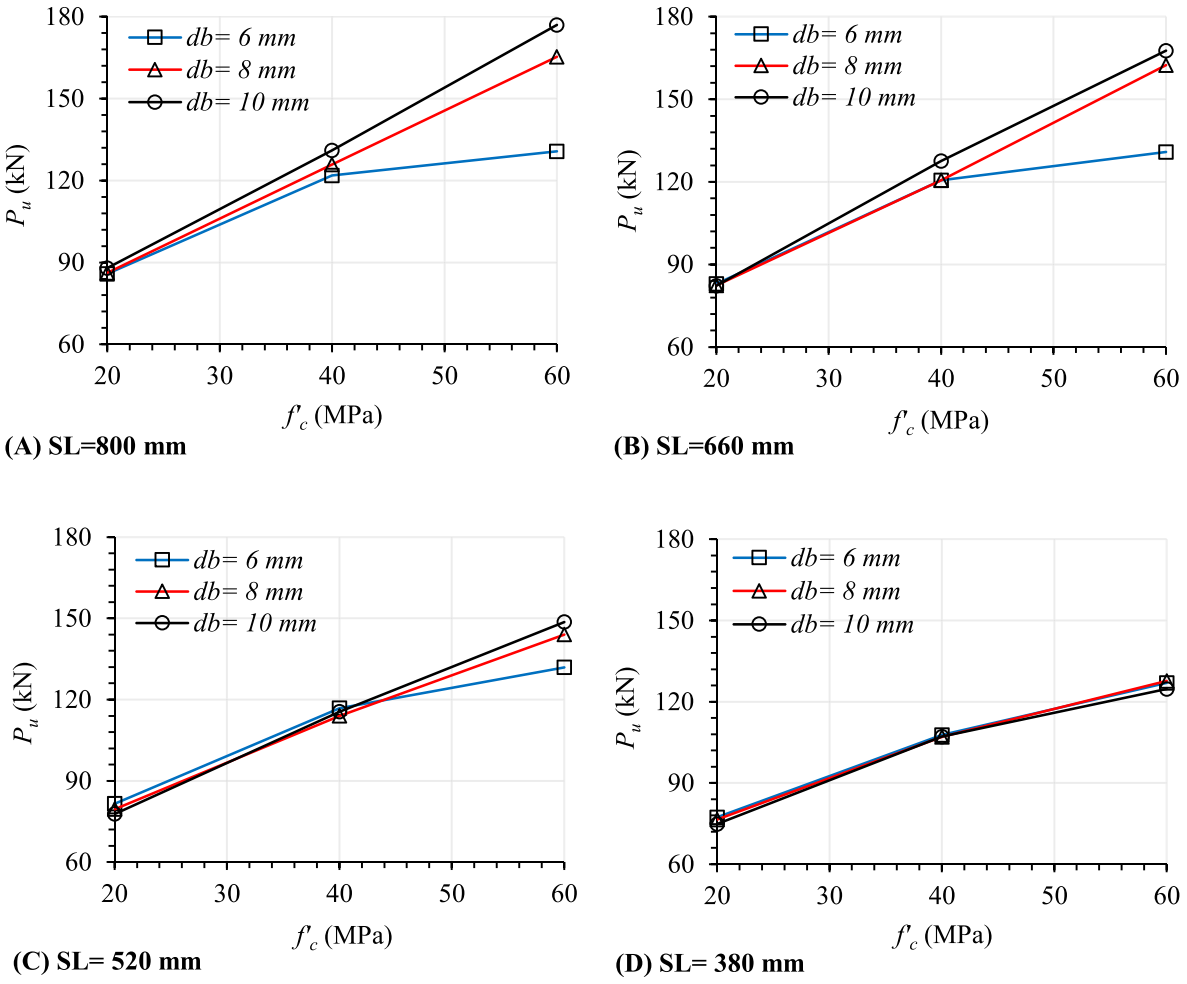

Fig. 11. Ultimate load (P_u) vs. concrete compressive strength (f_c') for various diameters of FRP bars (d_f) and strengthening length (SL).

ovoid repeatability and it showed the same trend for the effects of SL and SL_{eff} that was observed for $\rho_s = 0.0062$.

5.3. Effects of f_c'

Besides $f_c' = 40$ MPa that was used thus far, two values of 20 and 60 MPa, are used in this section to investigate the concrete strength which has significant effects on the bond-slip model for NSM FRP bars, concrete crushing, and peel-off failures, and the beam capacity. Fig. 11 plots the relation between P_u and f_c', for various d_f and SL values, and $h_g = 42$ mm. The figure shows that P_u increases significantly as f_c' increases with a rate of increase affected by FRP bar diameter and length. In average, P_u increased linearly by 167%, 187%, 204%, and 201% when f_c' increased from 20 to 60 MPa, when d_f was either 8 or 10 mm, and SL was 380, 520, 660, and 800 mm, respectively. For the small 6 mm bar diameter, the increase in P_u was slowed at f_c'40 to 60 MPa, likely due to the shift in failure mode from concrete peel-off to crushing at larger SL (e.g. 520, 660, and 800 mm).

5.4. Discussion on ductility

The ductility index (μ), defined as the ratio between the deflection at ultimate and that at steel yielding, is a valuable measure of the member's ability to sustain permanent deformations without sudden failure. While previous sections evaluated capacity and failure modes, this part examines the effects of S-NSM FRP reinforcement on the ductility of RC beams. Table 3 lists the ductility indices for strengthened beams for various SL, d_f, h_g, ρ_s values and f_c'=40 MPa. In Fig. 12, the relation between μ and SL is plotted, for various d_f and h_g values, with $\rho_s = 0.0062$ and f_c'=40 MPa. μ can be seen to be decreasing with the decrease of SL (Table 3), likely due to the brittle peel-off failure associated with short FRP bar lengths. Also, the bar diameter has adverse effects on ductility, where smaller d_f seem to result in higher μ than larger ones. μ seems to increase with h_g, but the trend is not consistent for all elevations due to coupling effects of d_f and SL, and the governing failure mode. Decreasing ρ_s from 0.0062 to 0.0027 results in a significant increase in ductility for most cases as seen in Table 3. In general, S-NSM FRP technique seems to furnish adequate ductility, resulting in a minimum, average, and maximum μ of 1.16, 2.73, and 4.76 for $\rho_s = 0.0027$ and similar respective values of 1.08, 2.30, and 3.65 for $\rho_s = 0.0062$.

5.5. Discussion on SL_{eff}

Following the discussion and methodology presented in section 5.1, SL_{eff} was estimated for multiple samples as the bar length where the load plateauing occurs. In some specimens, there was a small load increase at the transition from the linearly increasing curve where in these cases SL_{eff} was estimated as the bar length at which the increase in P_u between two successive points is less than 10%. In other specimens, P_u was still linearly increasing even when the bar length was equal to the beam span, due to the interaction of multiple failure modes, and thus SL_{eff} was not possible to extract. After estimating SL_{eff} values, a regression analysis was performed to relate its dependence to the variables considered in the parametric study and find a simple formula that can be used for

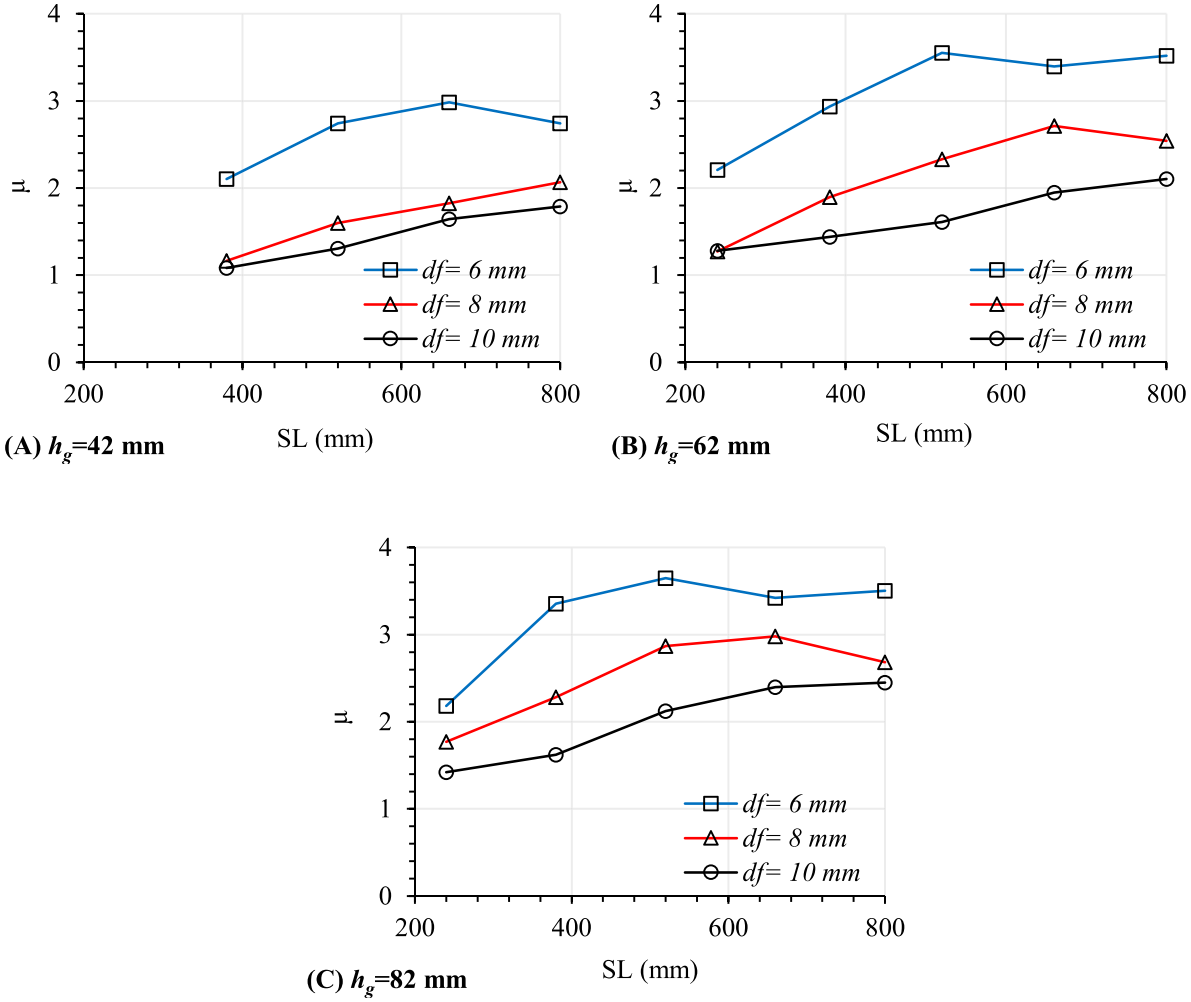

Fig. 12. Ductility index (μ) vs. strengthening length (*SL*) for various FRP bar diameters (d_f) and grooves heights (h_g).

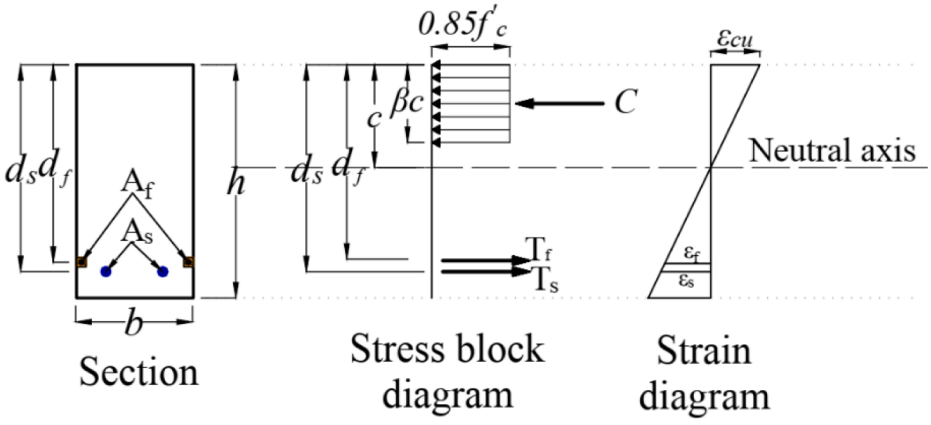

Fig. 13. Diagram of stresses and strains in a section of S-NSM FRP strengthened RC beams.

design purposes. The following equation was derived as best fit for SL_{eff} of S-NSM FRP system and it resulted in an excellent agreement with corresponding FE results, yielding a mean of 1.00 and a standard deviation of 0.07.

$$SL_{eff} = 193\left(\frac{h_g}{h}\right)^{-0.25} \rho_s^{-0.33} d_f^{0.57} f_c'^{-0.62} \quad (12)$$

6. Analytical model

For the technique to become widely used in retrofit applications, a reliable design model is required to accurately predict the member capacity at different potential failure modes. This section focuses on calculating analytically the flexural capacity of RC beams strengthened in flexure with S-NSM FRP bars, considering the failure modes and variables examined in the parametric study. The model presented in

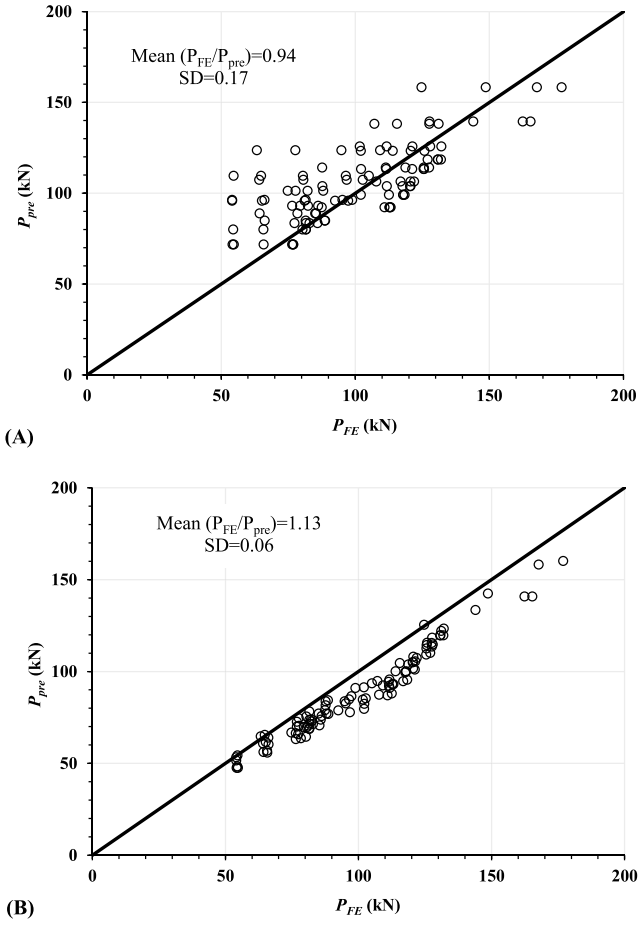

Fig. 14. Comparison between ultimate loads obtained from FE (P_{FE}) and preductions (P_{pre}) for: (A) Abdallah et al. and (B) current study.

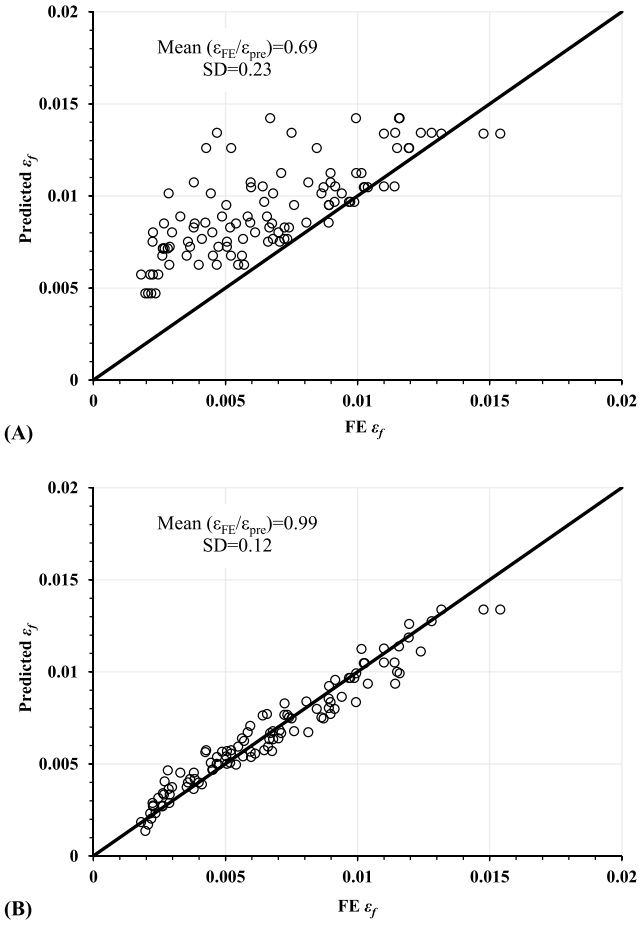

Fig. 15. Comparison between maximum strain in FRP bars obtained from FE (FE ε_f) and preductions (Predicted ε_f) for: (A) Abdallah et al. and (B) current study.

[33], based on the section analysis concept, is discussed and evaluated first. An improved model, considering the effects of concrete peel-off failure and effects of various parameters studied in this work on FRP strain, is presented and is shown to yield much better predictions than those from [33].

6.1. Abdallah et al. [27] model

For S-NSM FRP strengthened RC beams, capacity (P_u) of simply supported members with four-point load, can be related to their moment capacity (M_u) according to Eq. (13):

$$M_u = \frac{P_u}{2} \times a \tag{13}$$

where a is the distance between the applied point load and support (in current study $a = 800mm$).

The problem proceeds by calculating M_u from force equilibrium and strain compatibility principles and using adequate material constitutive models for each component [33]. Accompanying the calculations, Abdallah, Al Mahmoud [33] made the following assumptions: (1) perfect bond between concrete and steel or FRP reinforcements, (2) tensile strength of concrete is neglected, (3) ACI-318-19 [39] approximate stress–strain models are adopted for concrete and steel, (4) the beam fails by concrete crushing preceded by yielding of tensile steel. With the forces acting on the beam cross-section as shown in Fig. 13, M_u can be expressed as per Eq. (14):

$$M_u = A_s f_y \left(d_s - \frac{\beta c}{2}\right) + \varepsilon_f A_f E_f \left(d_f - \frac{\beta c}{2}\right) \tag{14}$$

whereA_s = area of the longitudinal steel reinforcement; f_y= yield strength of steel; d_s= effective depth of tensile steel calculated from the extreme compression fiber to the centroid of the tensile reinforcement; β= factor relating the depth of the equivalent rectangular compressive stress block to the neutral axis depth (c); ε_f= strain in FRP bars; A_f = area of S-NSM FRP bars; E_f= FRP elastic modulus; andd_f = effective depth for FRP bars.

While several other downstream equations are needed to produce a final solution for M_u, they are not shown here for brevity but can be viewed in Abdallah, Al Mahmoud [33] study or many other articles [10,12,28,31,41]. Predictions of Eq. (13) and (14) for P_u ($P_{u(pre)}$) are plotted in Fig. Fig. 14 (A) and 15 (A) and compared with the corresponding FE results ($P_{u(FE)}$). Fig. 14 (A) shows that predictions from the conventional analytical model are un-conservative particularly for short SL values, likely because of the brittle peel-off failure that is not considered in the model. Fig. 15 (A) plots the relation between maximum FRP strain at failure (ε_f) determined according to the section analysis model (predicted ε_f) (Eq. (13) and (14)) and that obtained from the FE analysis (FE ε_f) and shows a similar conclusion as to that given in Fig. 14 (A) regarding the un-conservativeness and results scatter of Abdallah, Al Mahmoud [33] model.

6.2. Proposed model

The section analysis-based model (Eq. (13) and (14)) needs further modifications to improve its predictions of P_u for S-NSM FRP strengthened beams. The extensive parametric FE study, totaling 108 models,

was used in regression analysis to determine the effects and significance of studied parameters (SL, d_f (taken as a ratio ρ_f), h_g, ρ_s, $f_c^{'}$) on (ε_f). The following equation, with an R^2 of 0.96, was derived for ε_f:

$$\varepsilon_f = 1.8 \times 10^{-8} SL^{0.72} \left(\frac{h_g}{h}\right)^{0.4} \rho_f^{-0.68} f_c^{'1.3} \quad (15)$$

where $\frac{h_g}{h}$ = ratio between groove elevation (h_g) and beam height (h), and other variables defined in previous sections.

Fig. 15 (B) shows that ε_f predicted by Eq. (15) is in close agreement with the FE-based ε_f, resulting in a Mean ($\varepsilon_{f(FE)}/\varepsilon_{f(pre)}$) of 0.99 and Standard Deviation (SD) of 0.12, compared to a Mean of 0.69 and SD of 0.23 for ε_f predicted by Eq. (13) and (14) using the conventional section analysis model proposed in [33]. Fig. 14 (B) shows the relation between P_{pre} and P_{FE}. where the former is calculated (also from section analysis) but using ε_f from Eq. (15) instead from the procedure given in [33]. The Mean and SD for $P_{u(FE)}/P_{u(pre)}$ where $P_{u(pre)}$ is calculated using ε_f from Eq. (15) were 1.13 and 0.06, respectively; compared to 0.94 and 0.17 for $P_{u(FE)}/P_{u(pre)}$ calculated with $P_{u(pre)}$ from conventional section analysis. The better predictions from the proposed model are likely due to considering concrete peel-off failure in the FE analysis and including the effects of key parameters (from Section 5) in the developed ε_f formula.

7. Conclusions

In this work, a robust FE model is developed to study the behaviour of RC beams strengthened with S-NSM FRP system. After validating with test results of 6 full-scale beam experiments, the model was used in an extensive parametric study evaluating the effects of multiple key parameters, namely: FRP bar diameter (d_f), strengthening length (SL), groove elevation (h_g), tensile steel reinforcement ratio (ρ_s), and concrete compressive strength ($f_c^{'}$). The following conclusions were extracted from the study:

1. The model captured the beam behavior with a good match for the load vs. deflection, load vs. steel strain, load vs. CFRP strain curves, and failure modes. It is divergence from test result for the ultimate load ranged from 0.94 to 1.03, with an average of 0.99 for all 6 beams.
2. Increasing d_f from 6 to 10 mm results in a consistent increase in the beam yielding and ultimate (P_u) loads, but negligible effects on stiffness. For each h_g, the effects of d_f on P_u seem negligible for short SL values but increase as SL increases, particularly for SL >520 mm.
3. Increasing SL from 240 to 800 mm for each d_f results in consistent and significant increase in ultimate load and ductility, with P_u of strengthened models increasing by 44 to 82%, relative to the control (un-strengthened) beam.
4. Doubling ρ_s from 0.27 to 0.62% resulted in an average increase in P_u by 31.4, 58.9, and 38.7% for h_g = 42, 62, and 82 mm and for all SL values, respectively. Using a ρ_s of 1.1% resulted in a failure change to shear due to over reinforcing the beam in flexure when combining the steel and FRP bars effects.
5. P_u increases significantly, by 167 to 201%, as $f_c^{'}$ increases from 20 to 60 MPa, with the rate of increase in P_u being mostly affected by FRP bar diameter and length.
6. The beam ductility index (μ) increases with the increase of SL, and the decrease in d_f and ρ_s. Average ductility for all S-NSM FRP strengthened beams was 2.73 and 2.3 for ρ_s = 0.27 and 0.62%, respectively, signifying the excellent performance of the system, likely due to its effects on reducing the brittle peel-off failure.
7. The effective length (SL_{eff}), beyond which levelling in load occurs due to a shift in failure mode away from the brittle concrete peel-off, is determined for the S-NSM FRP system based on regression analysis of FE results and presented in a mathematical formulation that considers the effects of h_g, ρ_s, d_f, and $f_c^{'}$.
8. A sectional analysis was also preformed, and an improved analytical model was presented for the ultimate load of S-NSM FRP strengthened RC beams, after deriving a regression-based formula for the FRP strain at beam failure which considers effects of key parameters.

Declaration of Competing Interest

The authors declare that they have no known competing financial interests or personal relationships that could have appeared to influence the work reported in this paper.

References

[1] Kaveh A, Behnam A. Optimal design of 3D reinforced concrete structures by charged system search considering frequency constraints. Scientia Iranica 2013;20:387–96.
[2] Kaveh A, Sabzi O. Optimal design of reinforced concrete frames using big bang-big crunch algorithm. Int J Civ Eng 2012;10(3):189–200.
[3] Kaveh A, Behnam AF. Cost optimization of a composite floor system, one-way waffle slab, and concrete slab formwork using a charged system search algorithm. Scientia Iranica 2012;19(3):410–6.
[4] Mottaghi L, Izadifard RA, Kaveh A. Factors in the relationship between optimal CO2 emission and optimal cost of the RC frames. Periodica Polytechnica Civ Eng 2021;65(1):1–14.
[5] Kaveh A, Izadifard R, Mottaghi L. Optimal design of planar RC frames considering CO2 emissions using ECBO, EVPS and PSO metaheuristic algorithms. J Build Eng 2020;28:101014.
[6] Kaveh A. Cost and CO2 emission optimization of reinforced concrete frames using enhanced colliding bodies optimization algorithm. In: Applications of Metaheuristic Optimization Algorithms in Civil Engineering. Springer; 2017. p. 319–50.
[7] Abdallah M, et al. Assessment of the flexural behavior of continuous RC beams strengthened with NSM-FRP bars, experimental and analytical study. Compos Struct 2020;242:112127.
[8] Abouzied A, Masmoudi R. Structural performance of new fully and partially concrete-filled rectangular FRP-tube beams. Constr Build Mater 2015;101:652–60.
[9] Jawdhari A. Behavior of rc beams strengthened in flexure with behavior of RC beams strengthened in flexure with spliced CFRP rod panels, in Civil Engnieering. 2016, Univeristy of Kentucky. p. 306.
[10] Kadhim MA, Jawdhari A, Peiris A. Evaluation of lap-splices in NSM FRP rods for retrofitting RC members. Structures 2021;30:877–94.
[11] American Concrete Institute (ACI). Guide for the design and construction of externally bonded FRP systems for strengthening concrete structures ACI 440.2R-17. Farmington Hills, MI; 2017.
[12] Hosen MA, Jumaat MZ, Alengaram UJ, Ramli Sulong NH. CFRP strips for enhancing flexural performance of RC beams by SNSM strengthening technique. Constr Build Mater 2018;165:28–44.
[13] Hosen MA, Jumaat MZ, Islam ABMS. Side Near Surface Mounted (SNSM) technique for flexural enhancement of RC beams. Mater Des 2015;83:587–97.
[14] Kadhim MMA, Adheem AH, Jawdhari AR. Nonlinear finite element modelling and parametric analysis of shear strengthening RC T-beams with NSM CFRP technique. Int J Civil Eng 2019;17(8):1295–306.
[15] Sabau C, Popescu C, Sas G, Schmidt JW, Blanksvärd T, Täljsten B. Strengthening of RC beams using bottom and side NSM reinforcement. Compos B Eng 2018;149:82–91.
[16] Zhang SS, Yu T, Chen GM. Reinforced concrete beams strengthened in flexure with near-surface mounted (NSM) CFRP strips: Current status and research needs. Compos B Eng 2017;131:30–42.
[17] Al-Mahmoud F, Castel A, Minh TQ, François R. Reinforced Concrete Beams Strengthened with NSM CFRP Rods in Shear. Adv Struct Eng 2015;18(10):1563–74.
[18] Al-Mahmoud F, Castel A, François R, Tourneur C. RC beams strengthened with NSM CFRP rods and modeling of peeling-off failure. Compos Struct 2010;92(8):1920–30.
[19] Al-Bayati G, Al-Mahaidi R, Hashemi MJ, Kalfat R. Torsional strengthening of RC beams using NSM CFRP rope and innovative adhesives. Compos Struct 2018;187:190–202.
[20] Obaidat YT, Ashteyat AM, Obaidat AT. Performance of RC beam strengthened with NSM-CFRP strip under pure torsion: experimental and numerical study. Int J Civ Eng 2020;18(5):585–93.
[21] Al-Bayati G, Al-Mahaidi R, Kalfat R. Experimental investigation into the use of NSM FRP to increase the torsional resistance of RC beams using epoxy resins and cement-based adhesives. Constr Build Mater 2016;124:1153–64.
[22] Badawi M, Soudki K. Flexural strengthening of RC beams with prestressed NSM CFRP rods – experimental and analytical investigation. Constr Build Mater 2009;23(10):3292–300.
[23] Foret G, Limam O. Experimental and numerical analysis of RC two-way slabs strengthened with NSM CFRP rods. Constr Build Mater 2008;22(10):2025–30.
[24] Shukri AA, Shamsudin MF, Ibrahim Z, Alengaram UJ. Parametric study for concrete cover separation failure of retrofitted SNSM strengthened RC beams. Mech Adv Mater Struct 2020;27(6):481–92.

[25] Imjai T, et al., Strengthening of damaged low strength concrete beams using PTMS or NSM techniques. Case Studies in Construction Materials, 2020. 13: p. e00403.
[26] Sharaky IA, Reda RM, Ghanem M, Seleem MH, Sallam HEM. Experimental and numerical study of RC beams strengthened with bottom and side NSM GFRP bars having different end conditions. Constr Build Mater 2017;149:882–903.
[27] Reda RM, Sharaky IA, Ghanem M, Seleem MH, Sallam HEM. Flexural behavior of RC beams strengthened by NSM GFRP Bars having different end conditions. Compos Struct 2016;147:131–42.
[28] Hosen MA, et al. Structural performance of lightweight concrete beams strengthened with side-externally bonded reinforcement (S-EBR) technique using CFRP fabrics. Compos B Eng 2019;176:107323.
[29] Salama ASD, Hawileh RA, Abdalla JA. Performance of externally strengthened RC beams with side-bonded CFRP sheets. Compos Struct 2019;212:281–90.
[30] Shukri AA, Hosen MA, Muhamad R, Jumaat MZ. Behaviour of precracked RC beams strengthened using the side-NSM technique. Constr Build Mater 2016;123:617–26.
[31] Hosen MA, Alengaram UJ, Jumaat MZ, Sulong NHR, Darain KMu. Glass Fiber Reinforced Polymer (GFRP) bars for enhancing the flexural performance of RC beams using side-NSM technique. Polymers 2017;9(12):180.
[32] Haddad RH, Yaghmour EM. Side NSM CFRP strips with different profiles for strengthening reinforced concrete beams. J Build Eng 2020;32:101772.
[33] Abdallah M, et al. Experimental study on strengthening of RC beams with Side Near Surface Mounted technique-CFRP bars. Compos Struct 2020;234:111716.
[34] ANSYS, Documentation for ANSYS. Release 17.2, 2016. Canonsburg, PA, USA.
[35] Jawdhari A, Adheem AH, Kadhim MMA. Parametric 3D finite element analysis of FRCM-confined RC columns under eccentric loading. Eng Struct 2020;212:110504.
[36] Willam KJ, Warnke EP, Constitutive model for triaxial behavior of concrete, in Proceedings of the international association of bridge and structural engineering conference. 1974, International Association of Bridge and Structural Engineering: Bergamo, Italy. p. 174-191.
[37] Kent DC, Park R. Flexural members with confined concrete. J Struct Div 1971;97(7):1969–90.
[38] Jawdhari A, Harik I. Finite element analysis of RC beams strengthened in flexure with CFRP rod panels. Constr Build Mater 2018;163:751–66.
[39] ACI, ACI 318-19: Building code requirements for structural concrete. 2019.
[40] Kadhim MM, Jawdhari A, Peiris A. Development of hybrid UHPC-NC beams: a numerical study. Eng Struct 2021;233:111893.
[41] Kadhim MM, Jawdhari A, Peiris A. Evaluation of lap-splices in NSM FRP rods for retrofitting RC members. Structures. Elsevier; 2021.
[42] Loreto G, Leardini L, Arboleda D, Nanni A. Performance of RC slab-type elements strengthened with fabric-reinforced cementitious-matrix composites. J Compos Constr 2014;18(3).
[43] Omran HY, El-Hacha R. Nonlinear 3D finite element modeling of RC beams strengthened with prestressed NSM-CFRP strips. Constr Build Mater 2012;31:74–85.
[44] Seracino R, Raizal Saifulnaz M, Oehlers D. Generic debonding resistance of EB and NSM plate-to-concrete joints. J Compos Constr 2007;11(1):62–70.
[45] CEB-FIB, Model code 1990: Design code. 1993: Thomas Telford Publishing.